NUMERICAL SIMULATION EXPERIMENTS ON THE LONG-TERM EVOLUTION OF A CO_2 PLUME UNDER A SLOPING CAPROCK

Karsten Pruess

Earth Sciences Division, Lawrence Berkeley National Laboratory
University of California, Berkeley, CA 94720
K_Pruess@lbl.gov

ABSTRACT

We have used the TOUGH2_MP/ECO2N code to perform numerical simulation studies of the long-term behavior of CO_2 stored in an aquifer with a sloping caprock. This problem is of great practical interest, and is very challenging due to the importance of multi-scale processes. We find that the mechanism of plume advance is different from what is seen in a forced immiscible displacement, such as gas injection into a water-saturated medium. Instead of pushing the water forward, the plume advances because the vertical pressure gradients within the plume are smaller than hydrostatic, causing the water column to collapse at the plume tip. Gas saturations and updip CO_2 fluxes are nearly constant, independent of time and position, in the upper, mobile portions of the plume. The CO_2 plume becomes thinner as it advances, yet the speed of advancement remains constant over the entire simulation period of up to 400 years, with migration distances of more than 80 km. Our simulation includes dissolution of CO_2 into the aqueous phase and associated density increase, and molecular diffusion. However, no convection develops in the aqueous phase because it is suppressed by the relatively coarse (sub-)horizontal gridding required in a regional-scale model. A first crude sub-grid-scale model was implemented to represent convective enhancement of CO_2 dissolution. This process is found to greatly reduce the thickness of the CO_2 plume, but does not affect the speed of plume advancement.

1. Introduction

Geologic storage as a greenhouse gas mitigation strategy will be workable only if long-term secure containment of CO_2 can be assured. At typical subsurface temperature and pressure conditions in terrestrial crust, separate-phase supercritical CO_2, henceforth for simplicity referred

to as "gas," is less dense than aqueous phase. It will thus experience an upward buoyancy force, and will tend to migrate towards shallower depth whenever suitable permeable pathways are available.

As the CO_2 plume spreads out under a caprock, it will become partially immobilized by capillary force ("trapped gas;" Kumar et al., 2004), while also partially dissolving in the aqueous phase. CO_2 dissolution functions as a gateway towards potential eventual fixation of CO_2 as carbonates of low solubility, and it induces a small increase in aqueous phase density, thus alleviating concerns about upward buoyancy flow. The progression from free gas to trapped gas, aqueous phase dissolution, and precipitation of solid carbonates increases CO_2 storage security (Fig. 1), and the quantitative aspects of CO_2 inventories and characteristic times involved are of great practical interest.

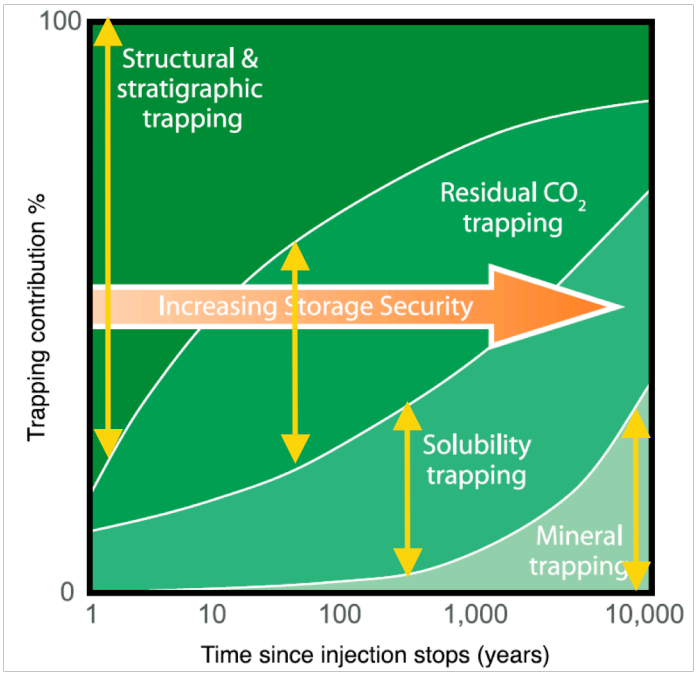

Figure 1. Progression of CO_2 storage modes over time (adapted from IPCC, 2005).

In this report we consider the long-term evolution of a large CO_2 plume that is emplaced beneath a sloping caprock. Our focus is on understanding the role and significance of different multi-phase, multicomponent flow and transport processes, including the rate of advance of the

CO_2 plume, mechanisms of gas and water flow, and CO_2 transport and inventory in gas and aqueous phases. Our model system is patterned after geometric dimensions and hydrogeologic parameters of the Carrizo-Wilcox aquifer in Texas, but problem specifications are intentionally simplified and idealized. We neglect chemical interactions between CO_2 and rock minerals.

The evolution of the CO_2 plume is determined by an interplay of different processes that operate on different space and time scales. From a numerical simulation viewpoint, it is extremely challenging to accurately represent all transport processes, because some require far more detailed spatial and temporal resolution than can be accomplished in regional-scale models. An example is the process of CO_2 dissolution-diffusion-convection (DDC): CO_2 overriding aqueous phase can dissolve and be transported away from the phase boundary by molecular diffusion. With increasing CO_2 concentrations, aqueous phase density increases by up to 1 %. This creates a gravitationally unstable configuration of denser aqueous phase above less dense, which may induce downward buoyant convection after some incubation time required for the diffusive boundary layer to grow to unstable width. Spatial resolution down to the cm-dm range would be required to resolve the initiation and growth of such convection, which is not practically feasible in regional-scale models. An important goal of our numerical simulation experiments is to obtain some estimation of corresponding space and time discretization errors, and to develop methods for improving the accuracy of process models. Possible techniques involve dynamic subgridding (Pau et al., 2009), or effective descriptions of sub-grid-scale processes.

2. Reference Case

2.1 Problem Parameters

The problem considered here is patterned after the Carrizo-Wilcox aquifer in Texas (Nicot, 2008; Hesse et al., 2008). We assume that a substantial number of CO_2 storage projects will be operating in the Wilcox, and we model a 2-D vertical section along the dip of the aquifer. The aquifer is modeled as a rectangular domain of 200 m thickness and 110 km length, tilted with an angle of $\alpha = 1.5^o$ against the horizontal (Fig. 2). We consider the upper right hand corner

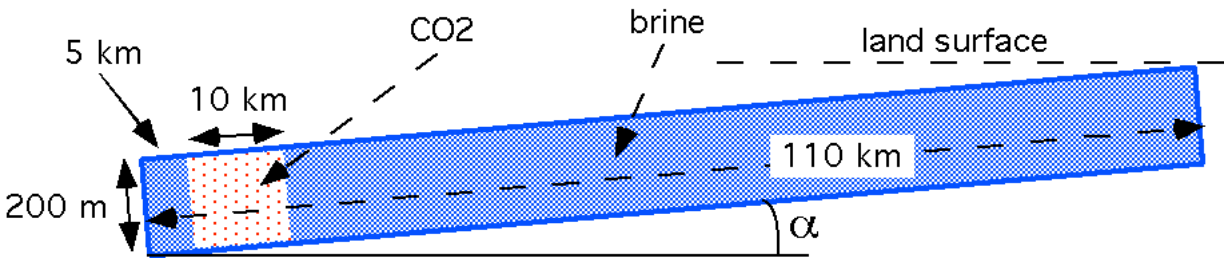

Figure 2. Geometric dimensions of the 2-D rectangular domain modeled. The domain is dipping upward by an angle α. The initial CO_2 plume is shown by light shading.

of the domain to be at the land surface; the lower left hand corner is then at a depth of 110,000 sin(α) + 200 cos(α), which for α = 1.5° corresponds to 3,079.4 m. Formation properties include a uniform and isotropic permeability of 500 mD, a porosity of 15 %, and a compressibility of 4.5×10^{-10} Pa^{-1} (similar to compressibility of water at ambient conditions). Boundary conditions are "no flow" everywhere, except that the upper right hand corner of the domain is held at land surface conditions of $(T_0, P_0) = (10\ ^\circ C, 1.013 \times 10^5\ Pa)$. The domain is initialized as a fully (fresh-) water-saturated medium in hydrostatic equilibrium, held in a geothermal gradient of 30 °C/km relative to a land surface temperature of 10 °C. The initialization is accomplished in two steps. First we use a free-standing utility program to read in a TOUGH2 MESH file and write out an INCON file with temperature and pressure data assigned as $T(Z) = T_0 + grad(T)*Z$, $P(Z) = P_0 + grad(P)*Z$. Here, Z is the true depth relative to a reference point with conditions (T_0, P_0), and an approximate value of $grad(P) \approx 10^4$ Pa/m is used. Subsequently we initialize a TOUGH2 simulation with these INCON data, maintaining temperatures at their initial values, and allowing pressures to come to an accurate gravitational equilibrium relative to a pressure of 1.013×10^5 Pa at the land surface.

The CO_2 plume is emplaced instantaneously by using another utility program to assign a uniform gas saturation of $S_g = 80$ %, corresponding to aqueous phase at irreducible saturation of $S_{lr} = 20$ %, to the subdomain labeled "CO_2" in Fig. 2; for the CO2 emplacement, pressures and temperatures are maintained at their initial values. Plume evolution takes place under the combined action of gravity and pressure forces, with CO_2 buoyancy due to lower density being the primary driving force. For the simulations reported here we neglect capillary pressures.

Effects of aqueous diffusion, and enhancement of CO_2 dissolution through convective mixing, are explored in sensitivity studies, see below. Relative permeabilities for liquid (k_{rl}) and gas (k_{rg}) were assumed as follows,

$$k_{rl} = \sqrt{S^*}\left\{1-\left(1-[S^*]^{1/m}\right)^m\right\}^2 \quad (1a)$$

$$k_{rg} = \left(1-\hat{S}\right)^2\left(1-\hat{S}^2\right) \quad (1b)$$

where $S^* = (S_l - S_{lr})/(1 - S_{lr})$, $\hat{S} = (S_l - S_{lr})/(1 - S_{lr} - S_{gr})$, with S_l the liquid (aqueous phase) saturation, and S_{lr}, S_{gr} the irreducible liquid and gas saturations, respectively. Eq. (1a) for liquid was developed by van Genuchten (1980); Eq. (1b) for gas is due to Corey (1954). Parameters used are $S_{lr} = S_{gr} = 20$ %, m = 0.457. The relative permeabilities given by Eq. (1) are non-hysteretic; problem variations with hysteretic relative permeabilities will be explored in the future (Doughty, 2007).

Obtaining accurate results for this problem, and interpreting simulated behavior, is made difficult by the extreme aspect ratio of the flow system. This is illustrated by the contour map of temperatures, Fig. 3. Temperatures are a function of depth only, so the isotherms shown in Fig. 3 are in fact horizontal. Additional difficulties arise from the multi-scale nature of the flow processes, effects of space and time discretization, and from orders-of-magnitude variations in mass fluxes in space and time.

CO_2 is introduced into the 10 km by 200 m large domain highlighted in Fig. 2 under conditions corresponding to the initial hydrostatic pressure equilibrium in a geothermal gradient. Due to its lower density as compared to aqueous phase, CO_2 experiences a buoyancy force that drives it upward, towards shallower depth. As had been mentioned, we hold temperatures constant at initial values throughout the simulation. Fig. 4 shows the variation of CO_2 density throughout the flow domain for the applied hydrostatic-geothermal conditions. (This figure does not represent simulation results for the CO_2 plume behavior; it simply shows the density that free-phase CO_2 would have throughout the domain.) Recall that (P, T)-conditions, hence CO_2 density, are functions of depth only. It is seen that the interplay of temperatures and pressures both increasing with depth is such that CO_2 density is nearly constant at around 650 kg/m^3 in the

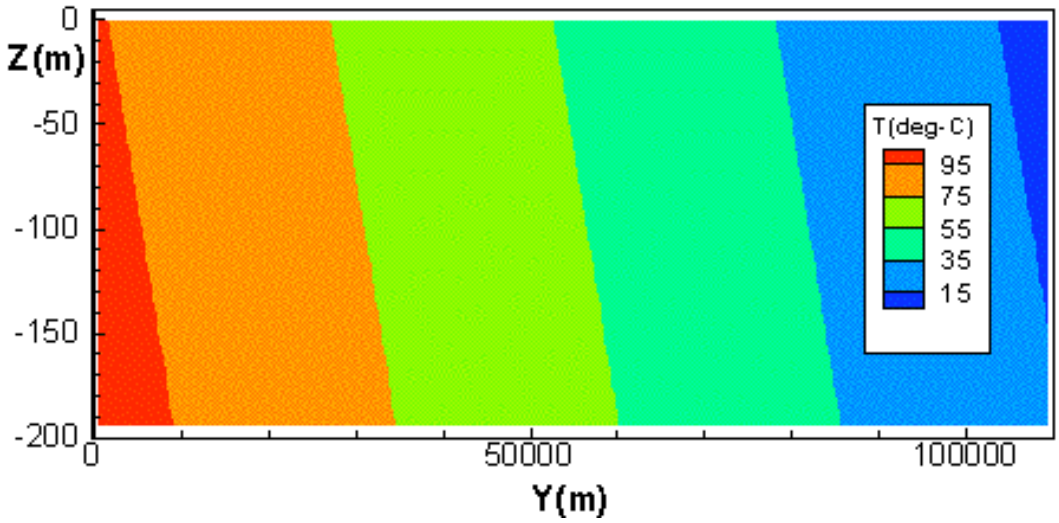

Figure 3. Temperatures corresponding to a geothermal gradient of 30 ºC per km depth, and a land surface temperature of 10 ºC. Temperature is a function of depth only, so that isotherms are actually horizontal.

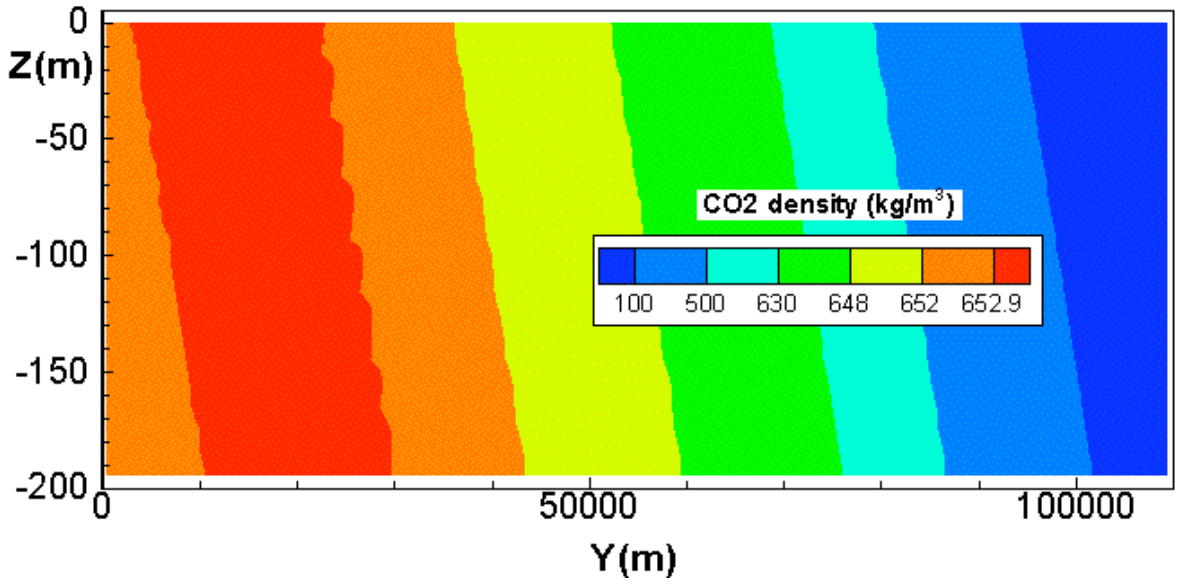

Figure 4. Variation of the density of free-phase CO_2 throughout the model domain. Note that CO_2 density depends on temperature and pressure, both of which are a function of true depth only.

deeper portions of the aquifer. This implies that the buoyancy force experienced by CO_2 in a hydrostatic pressure field is nearly the same throughout the deeper regions. Only for Y > 70 km, corresponding to true depths less than 1,047 m, is CO_2 becoming noticeably less dense. As will be seen below, CO_2 flow effects produce only modest perturbations of the initial hydrostatic pressure field, so that the CO_2 densities plotted in Fig. 4 are relevant for the actual plume evolution.

The evolution of the CO_2 plume was modeled with a parallelized version of our general-purpose reservoir simulator TOUGH2 (Pruess, 2004; Zhang et al., 2008), augmented with a fluid property module ECO2N that provides accurate correlations for thermophysical properties of fluids, including the partitioning of H_2O and CO_2 between brine and gas phases (Pruess and Spycher, 2007). The basic space discretization was 10 m in the sub-vertical and 1000 m in the sub-horizontal direction, but we did some experimentation with grid refinement to achieve a compromise between spatial resolution and efficient execution. Most of the simulations presented here were done with a grid that involved refinement to $\Delta Z = 1$ m near the top, to better resolve the CO_2 plume, as well as refinement to $\Delta Y = 10$ m in the Y-direction near Y = 50 km (Fig. 5). The latter refinement was done to be able to monitor plume advancement with a spatial resolution down to 10 m, and thereby obtain a more accurate depiction and understanding of flow mechanisms at the advancing phase front. The MESH has 7300 grid blocks. All simulations were performed on a Dell T5400 dual quad core computer with a total of eight cores. For parallelized execution, we would normally partition the simulation domain into eight subdomains, and assign each processor core the computations corresponding to one subdomain. However, in most cases we partitioned the computations into 16 parallel processes (two per processor), as this was found to reduce execution time compared to running eight processes. Individual runs typically took about 1 to 1.5 hours.

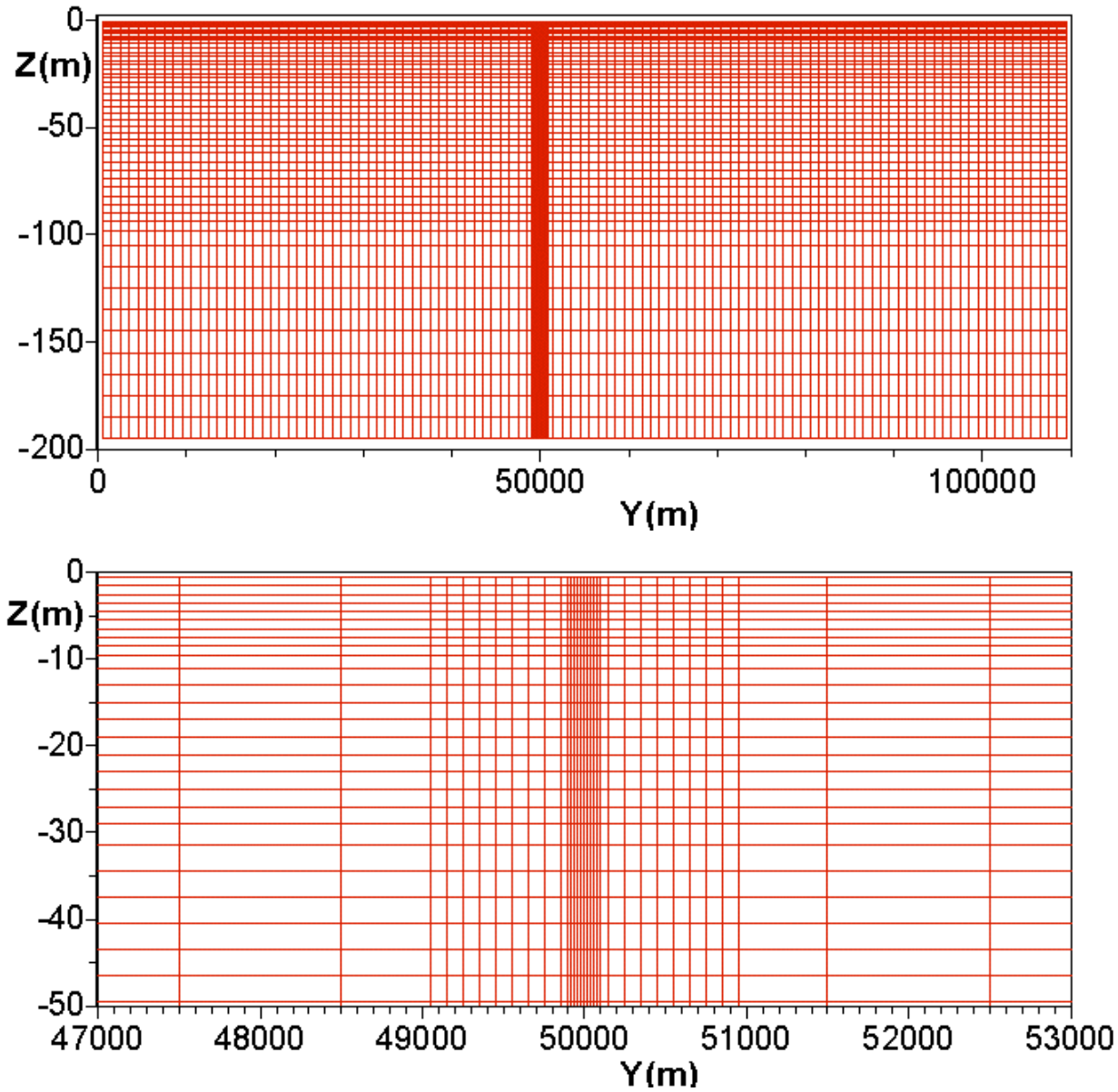

Figure 5. Computational grid showing the entire flow system (top) and a zoom into the region with refined gridding (bottom).

2.2 Results for Gas Phase

Of main interest is the behavior of free-phase CO_2. Fig. 6 shows gas saturations at three different times, indicating that the plume thins out as it migrates under the sloping caprock. Mass flows of CO_2 generally decrease with distance from the original CO_2 emplacement, and one

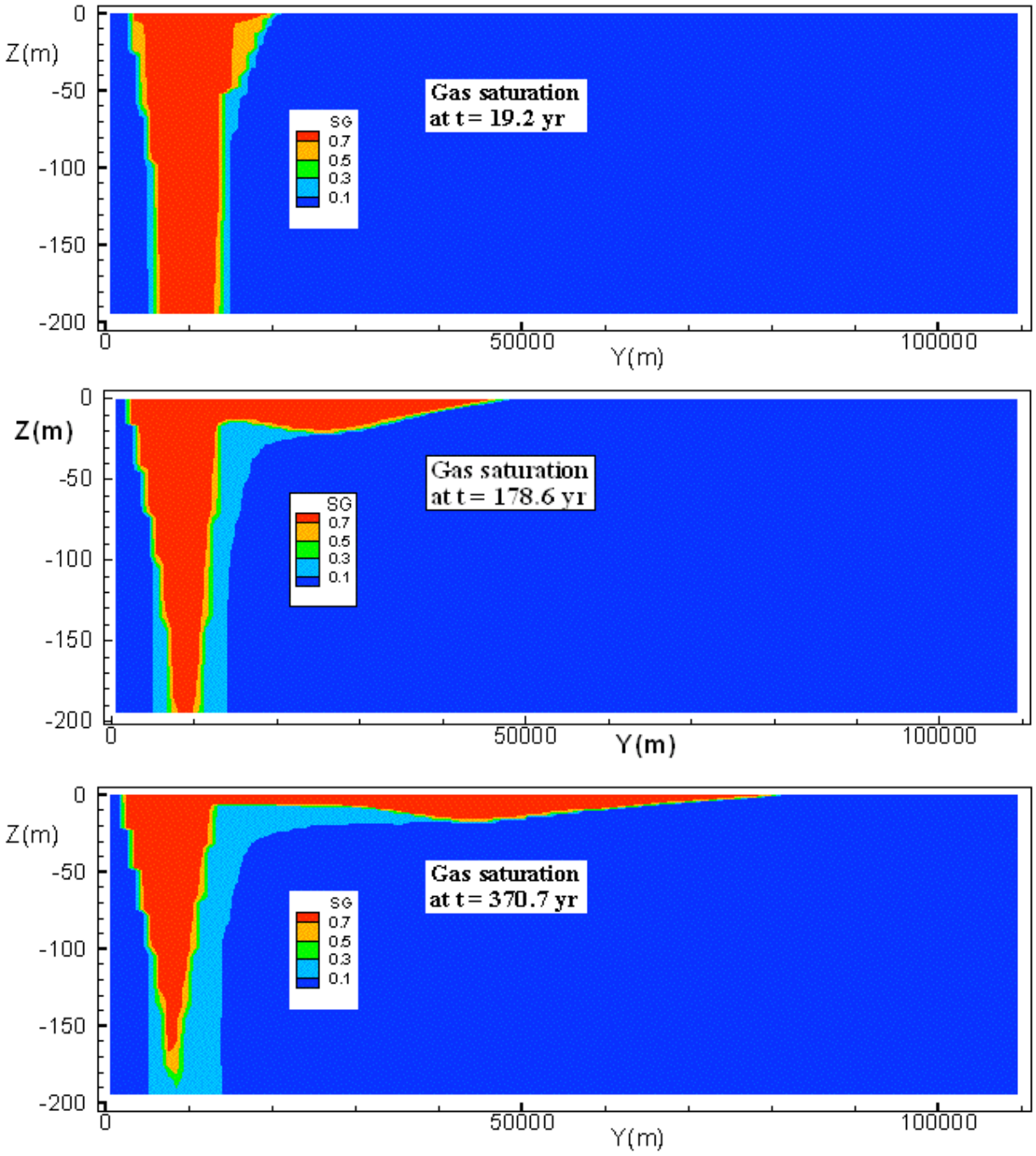

Figure 6. Simulated gas saturations at different times.

may expect that the advancement of the plume may slow over time. This, however, is not the case. Fig. 7 shows that the plume does advance more rapidly for a brief initial period, due to the strong driving force provided by the initial placement of the CO_2 plume in a hydrostatic pressure

field. However, subsequent advancement of the plume occurs with constant speed. The small scatter of points about the eye-fitted straight line is due to space and time discretization effects. At different times, we identify the location of the front by the outermost grid block in Y (updip) direction that has reached two-phase conditions. Gas saturations in the outermost block can have a range of values, corresponding to different times in the desaturation cycle, which explains the scatter seen in Fig. 7. From the slope of the eye-fitted straight line, we deduce an average speed of plume advancement of $V_p = (82\text{-}17.5)\text{x}10^3/12\text{x}10^9 = 5.375\text{x}10^{-6}$ m/s (169.6 m/yr). The speed of plume advance is given by the pore velocity of CO_2 at the front. Its near-constancy can be understood by noting that (1) the plume advances with a constant frontal saturation,

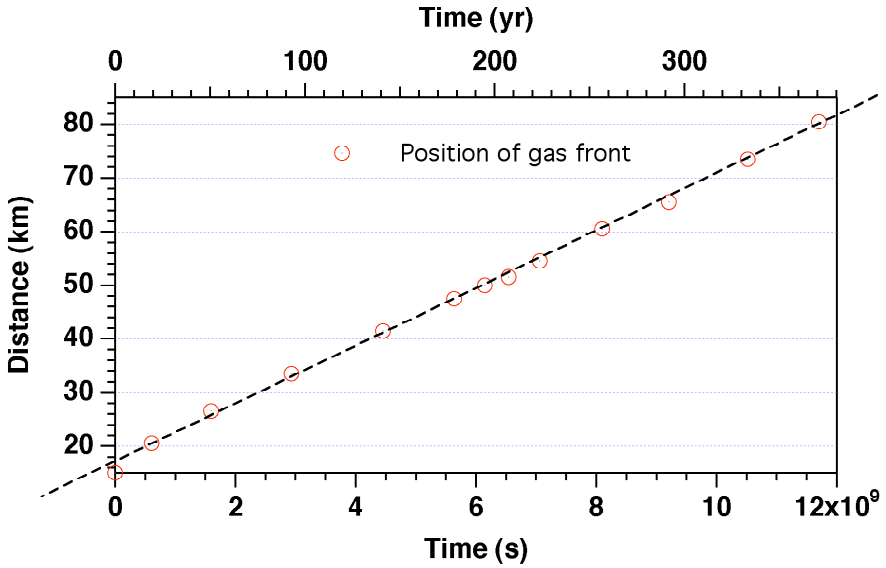

Figure 7. Advancement of the gas front over time. Distance is measured with respect to the l.h.s. of the domain, so that at time t = 0, the plume extends to Y = 15 km. The dashed line is an eye fit that ignores the brief initial period with more rapid advancement before the second data point.

corresponding to constant relative permeability and fluid mobility, (2) the pressure field remains close to hydrostatic, and (3) CO_2 density, hence buoyancy force in a given pressure gradient, is nearly independent of position (depth). The simulated migration speed can be quantitatively explained by considering the motion of an immiscible blob of CO_2 with density difference $\Delta\rho$ in a hydrostatic pressure field. The volumetric flux of such a blob would be given by $v = k\left(k_{rg}/\mu_g\right)\Delta\rho g$, and the component along the slope of a caprock tilted by an angle θ would be $v\sin\theta$. The corresponding pore velocity would be

$$V_{pore} = \frac{k k_{rg} \Delta\rho g}{\phi S_g \mu_g} \sin\theta \qquad (2)$$

Inserting parameters applicable for our problem from Table 1, we obtain V_{pore} = 170.5 m/yr, in excellent agreement with the value of 169.6 m/yr read off the slope of the straight line in Fig. 7. Hesse et al. (2008) performed a detailed analysis of plume migration in a vertically-averaged sharp interface model. It can be shown that for the advancement of the plume tip, their model reduces to Eq. (2). However, the model of Hesse et al. assumes gas saturation to be $S_g = 1 - S_{lr}$ throughout the plume, or S_g = 80 % for our parameters. This results in about 30 % larger gas relative permeability, so that the predicted speed of plume advancement is then somewhat larger also, namely 221.1 m/yr.

Table 1. Data used for evaluating pore velocity from buoyancy flow from Eq. (2).

permeability	$k = 500 \times 10^{-12}$ m^2
porosity	ϕ = 15 %
gas saturation in plume	S_g = 73 %
gas relative permeability from Eq. (1b)	$k_{rg}(S_g = 0.73) = 0.771$
gas phase viscosity	μ_g = 0.525x10-4 Pa-s
gas density at (T, P) = (55 ºC, 150 bar)	ρ_g = 654.957 kg/m^3
water density at (T, P) = (55 ºC, 150 bar)	ρ_l = 992.138 kg/m^3
density difference	$\Delta\rho$ = 337.181 kg/m^3
tilt	$\sin\theta = \sin 1.5^o = 0.02618$
gravitational acceleration	g = 9.81 m/s^2

The nearly constant gas phase density together with nearly constant pore velocity further implies that the sub-horizontal component of CO_2 mass flux is nearly independent of position. Accordingly, the total CO_2 mass flow rate in the direction of plume migration must decrease in proportion to the plume thickness.

Fig. 8 gives a more detailed view of the gas plume, indicating that gas saturations are nearly constant throughout at $S_g \approx 73\%$ in the upper portions of the plume. Sub-horizontal pore velocities V_{pore} of gas are nearly constant as well, as expected, showing only small variations about the average speed $V_p = 5.38 \times 10^{-6}$ m/s (169.6 m/yr) of plume advancement (Fig. 9). There are some minor variations in V_{pore} with a distinct spatial pattern; as no such patterns are visible in

the gas saturations (Fig. 8), these must be due to (small) spatially correlated variations in pressure gradients. Fig. 8 also indicates that the thickness of the plume behind the tip, hence the total CO_2 mass flow rate, increases approximately linearly with distance from the tip. At larger distance behind the plume tip, the thickness of the mobile plume is reduced, and beneath the mobile portion is a region of considerable thickness in which gas saturation is near the irreducible limit of 0.2 (Fig. 8). This region had been swept by CO_2 at earlier time, and subsequently has been depleted of mobile CO_2 by slow upflow in a vertical gradient that is intermediate between gas-static and hydrostatic.

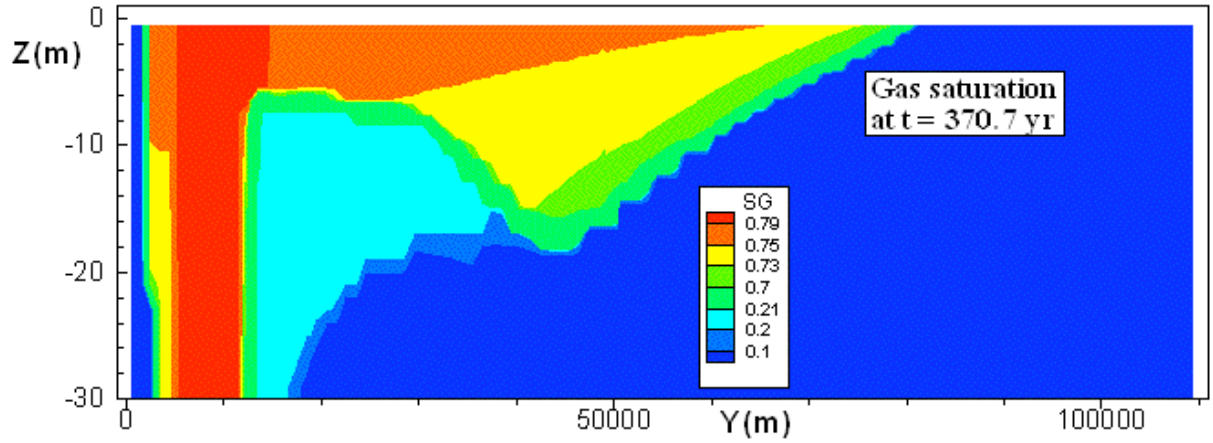

Figure 8. Detailed view of gas saturations near the top boundary. Note the extreme vertical exaggeration.

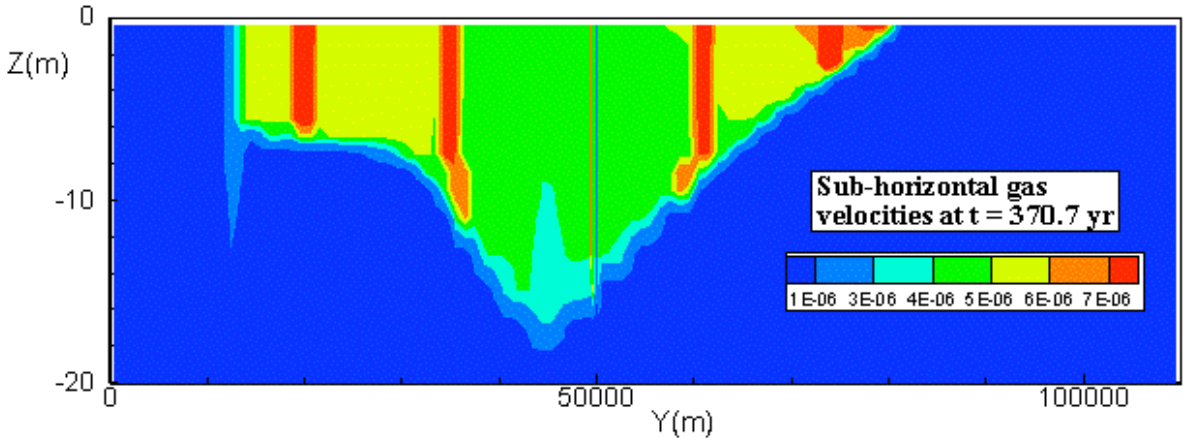

Figure 9. Sub-horizontal gas phase pore velocities at a time of 370.7 yr. Note the extreme vertical exaggeration.

The time dependence of gas flux and gas saturation in the center of the more finely gridded region near Y = 50 km, at the top of the flow domain, is shown in Fig. 10. Gas is beginning to cross the Y = 50 km interface after 6.15×10^9 s (194.8 yr), and gas saturation in the upstream block located at Y = 50,005 m quickly rises above $S_g = 0.7$. Subsequent local maxima in gas flux reflect space discretization effects, and correspond to the gas plume advancing into the second, third, etc. row of grid blocks from the top. Additional discussion of the transient changes involved in the plume advance is given in the section on aqueous phase, below.

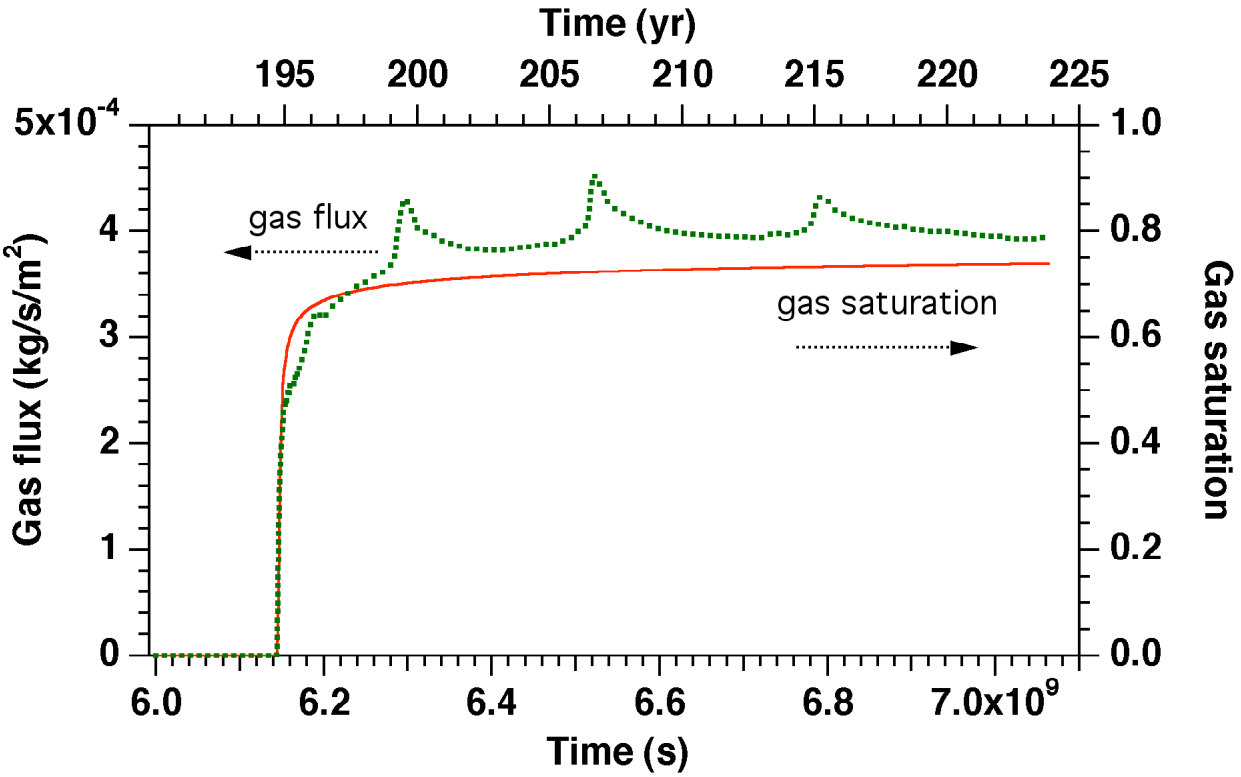

Figure 10. Sub-horizontal gas flux and saturation transients at the top of the flow domain, Y = 50 km.

2.2 Results for the Aqueous Phase

The aqueous phase plays a four-fold role in affecting the evolution of the CO_2 plume, (1) it serves as a medium for pressure transmission, (2) it occupies pore space that must be vacated to enable advancement of the CO_2 plume, (3) it can solubilize CO_2, hence serve as a sink, and (4) it provides a transport medium for dissolved CO_2 by diffusive and advective processes. Aqueous phase in contact with free-phase supercritical CO_2 may dissolve on the order of 5 % by weight of

CO_2, less for saline brines. In the following discussion, we will refer to the aqueous phase often simply as "water" or “liquid.”

The ultimate equilibrium state between a gas plume above and aqueous phase below would involve the aqueous phase having dissolved a mass fraction of CO_2 corresponding to phase equilibrium at prevailing conditions of pressure, temperature, and salinity. For most of the flow domain considered here, equilibrium CO_2 mass fraction would be approximately 5.2 %. With a total initial aqueous phase inventory of 3.03×10^9 kg, such equilibrium would correspond to a total amount of dissolved CO_2 of 157.6×10^6 kg = 157.6 kt, which is almost exactly equal to the total initial CO_2 inventory of 158.7 kt. This indicates that the aqueous phase represents a very large potential sink, that can dissolve almost the entire CO_2 inventory. The critical issue is, how readily is this sink available, how fast is dissolution happening?

The large range of relevant spatial scales, and order-of-magnitude variations in water velocities, make water flow patterns difficult to visualize. Fig. 11 shows a snapshot of water pore velocities at $t = 6.15 \times 10^9$ s (194.8 yr), at which time the gas plume has advanced to Y = 50 km (Figs. 7, 10). The reason for picking this snapshot is that we have applied local grid refinement around Y = 50 km, making this a “preferred spot” for understanding water flow (Fig. 5). It is seen that there are large downward water velocities right at and beneath the gas front, which can be understood as follows. Due to the lower density of CO_2, vertical pressure gradients are less than hydrostatic throughout the plume. Water near the plume tip experiences this less-than-hydrostatic gradient, causing water to flow downward, and vacating pore space at the top of the permeable interval into which the CO_2 plume may advance. One could say that the groundwater column “collapses” as the CO_2 plume with its smaller (sub-) vertical pressure gradient approaches. This mechanism of gas invasion into the aqueous zone is quite different from what would be encountered near a CO_2 injection well, where a gas plume will advance by displacing water outward under a pressure gradient maintained by the injection operation. Fig. 11 shows that in the present problem, water is removed at the advancing gas front primarily by outward rather than by downward flow. This observation suggests that any impedance to vertical flow, such as from layers of lower permeability, should result in slowing the advance of the gas plume, even if such layers were beneath and away from the plume itself.

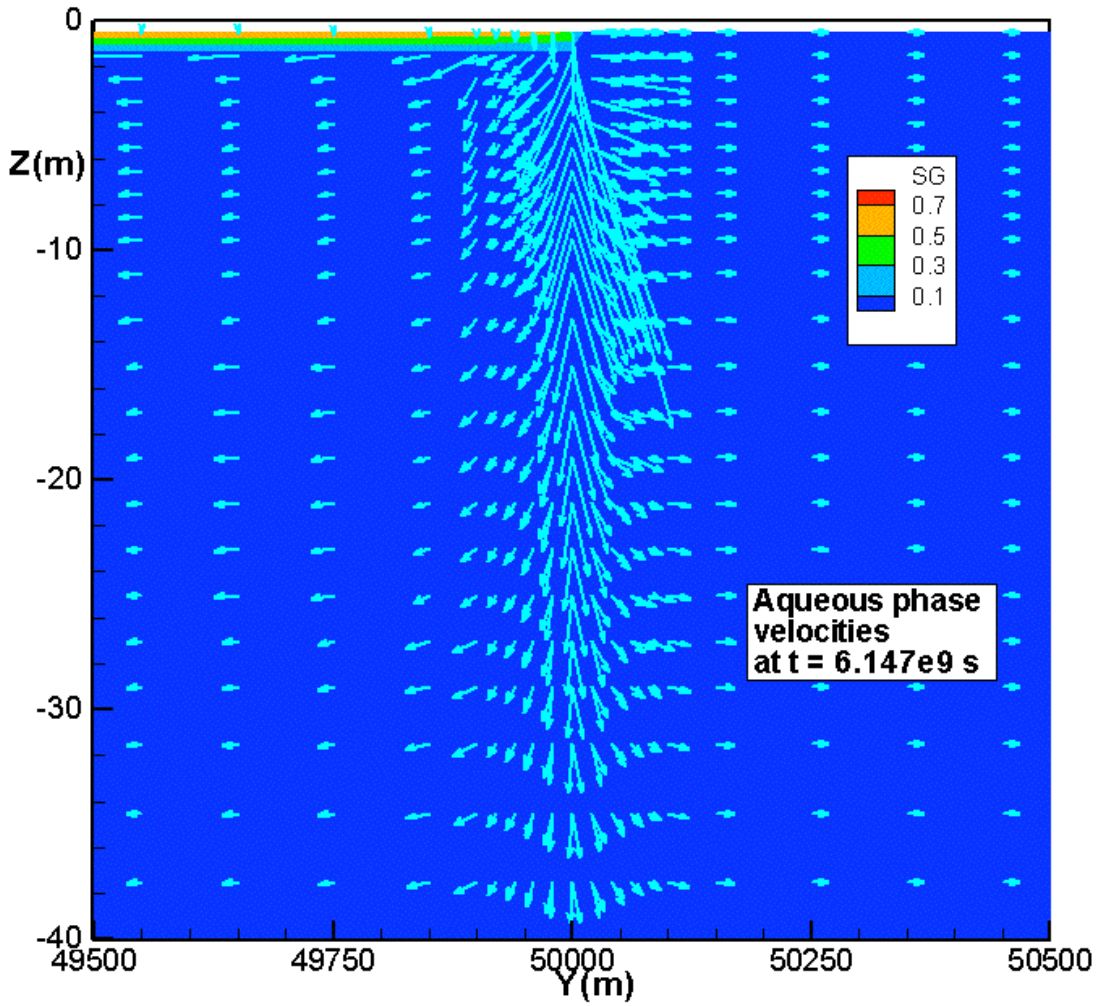

Figure 11. Aqueous phase velocities near the gas front at time t = 194.8 yr. The lengths of vectors are proportional to velocity.

Reducing vertical permeability k_v will have two different and distinct effects on plume evolution, as it (1) impedes the buoyant upflow of CO_2 in the main storage region, that feeds the lateral migration of the plume, and (2) impedes the downflow of water at the advancing gas front. Because of the much larger mobility of CO_2 as compared to water, we expect that limitations to water movement will be the dominant effect. Two numerical experiments were performed to test this hypothesis. In experiment A the reference case was rerun with vertical permeability reduced by a factor 10 throughout (from 500 to 50 mD), while in experiment B the vertical permeability in the region initially occupied by the CO_2 plume was maintained at 500 mD, while everywhere else it was reduced to 50 mD. Observed speeds of plume advancement were 5.38×10^{-6} m/s in the reference case, 4.45×10^{-6} m/s in experiment A, and 4.78×10^{-6} in

experiment B, representing a reduction by 17.3 % for experiment A, and a reduction by 11.2 % in experiment B. Thus most of the reduction in plume speed occurs even when vertical permeability in the initial plume region is maintained at a high value (experiment B), demonstrating that most of the reduction in plume speed arises from impediments to vertical flow of liquid, while impediments to vertical flow of gas in the initial plume region have lesser impact.

The downward water flow generates a flow divide in the aqueous phase, where behind the gas front aqueous phase flows downward and inward, towards the CO_2 plume, while beyond the gas front water flow is downward and outward, away from the plume. In the plume itself, water flow is small and downward (Fig. 12).

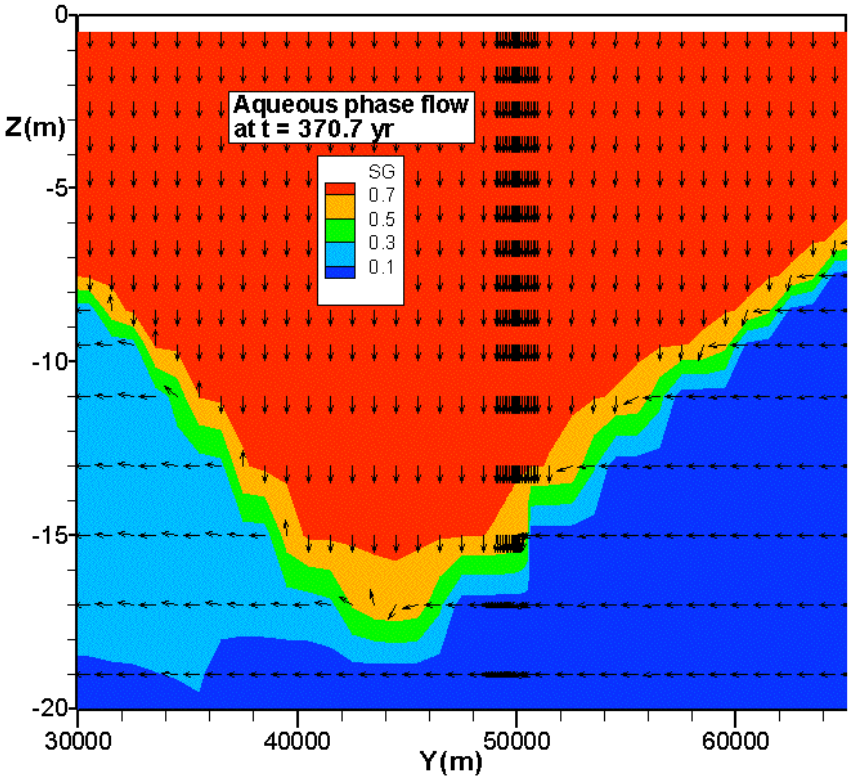

Figure 12. Aqueous phase flow after 370.7 years near the central portion of the gas plume. The vectors all have the same length and just indicate the direction of flow, not the magnitude of flow velocities.

Fig. 13 gives a large-scale view of the sub-horizontal (Y) component of aqueous pore velocity, showing a flow divide at the gas front Y = 80.5 km between leftward flow for Y < 80.5 km and rightward flow for Y > 80.5 km.

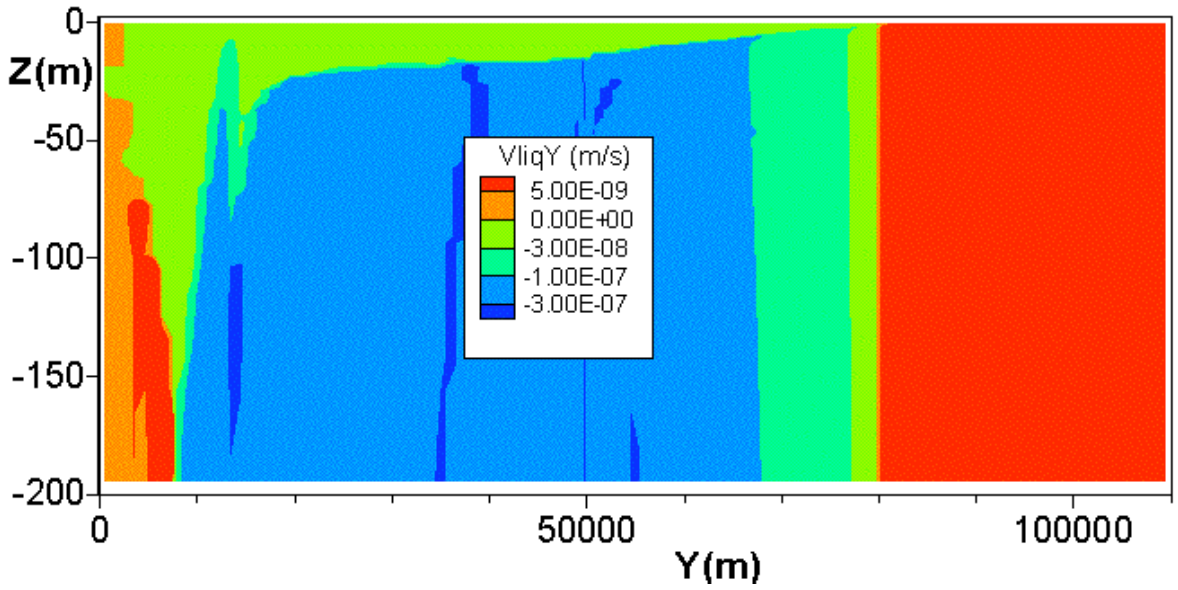

Figure 13. Sub-horizontal component of aqueous pore velocity at t = 370.7 years.

As had been seen above, the gas phase occupies only a thin layer at the top of the permeable interval. Nonetheless it has a profound effect on the evolution of pressures in the system, and thereby affects the movement of aqueous phase. Fig. 14 shows the changes in pressures relative to the original hydrostatic values after 370.7 years, at which time the leading edge of the gas plume is at Y = 80.5 km (Figs. 6, 8). Pressures are reduced for Y < 65 km, i.e., over most of the region over which the gas plume extends. Pressure reduction is strongest at the deepest elevations. If pressure changes were a function of depth, then their pattern would be aligned with the purely depth-dependent temperatures in Fig. 3. This is not the case; instead, pressure changes are essentially just a function of Y. In the region Y < 65 km this means that pressures at a given depth decrease towards the left (downdip), providing a driving force for water flow in this direction. The change pattern also implies that vertical pressure gradients are reduced relative to the original hydrostatic values. In fact, in the gas bubble itself pressure gradients tend towards gas-static, as appropriate for CO_2 density. This causes water to drain

downward in the gas bubble, over time approaching irreducible saturation. The region near the gas front (Y = 80.5 km after 370.7 yr) shows a pressure increase, and a reduction in the vertical component of pressure gradient. These observations explain why water flows downward at the leading edge of the plume, and flows towards the left for Y < 80.5 km, and to the right for Y > 80.5 km.

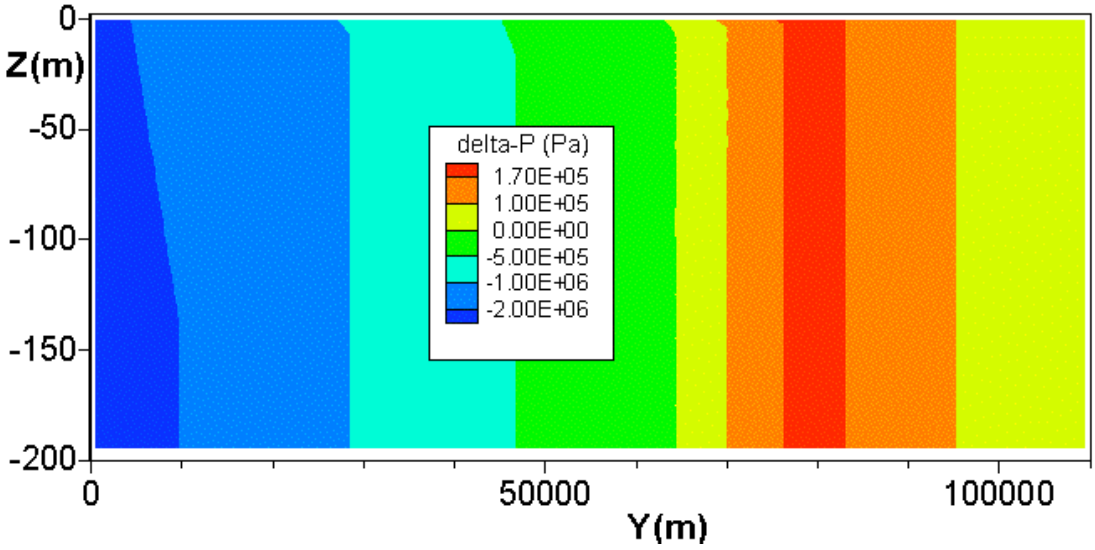

Figure 14. Simulated pressure changes over a period of 370.7 years.

To round out this discussion, we present the detailed time dependence of aqueous phase fluxes during passage of the gas front (Fig. 15). We consider the grid blocks located at Y = 49,995 and 50,005 m in the top row (vertical grid resolution ΔZ = 1 m). Before close approach of the gas front, (sub-) horizontal flux of aqueous phase is outward at a magnitude of approximately 10^{-6} kg/s/m^2. The flux increases with the approach of the gas front, reaching a maximum of 5.9×10^{-6} kg/s/m^2 just prior to the upstream block making a transition to two-phase conditions. After the transition to two-phase conditions in the upstream block, (sub-) horizontal aqueous phase flux decreases dramatically, and after a while changes direction, with aqueous phase flowing towards the advancing plume, albeit at very small rates. The more interesting behavior is in the (sub-) vertical flux of aqueous phase, which is downward (negative) at rates that increase dramatically with the approach of the gas front, reaching a maximum of 2.52×10^{-5} kg/s/m^2 at a time of $t = 6.147 \times 10^9$ s (194.8 yr), when the rate of desaturation in the top grid block located at Y = 50,005 m is most rapid. By integrating the simulated downward aqueous phase flow from this

block over time we can calculate the cumulative voidage of pore space; we find that this accounts quantitatively for the simulated increase in gas saturation. This is further confirmation that it is indeed the downward flow of aqueous phase that enables the advancement of the gas front, with (sub-) horizontal flow playing only a minor role.

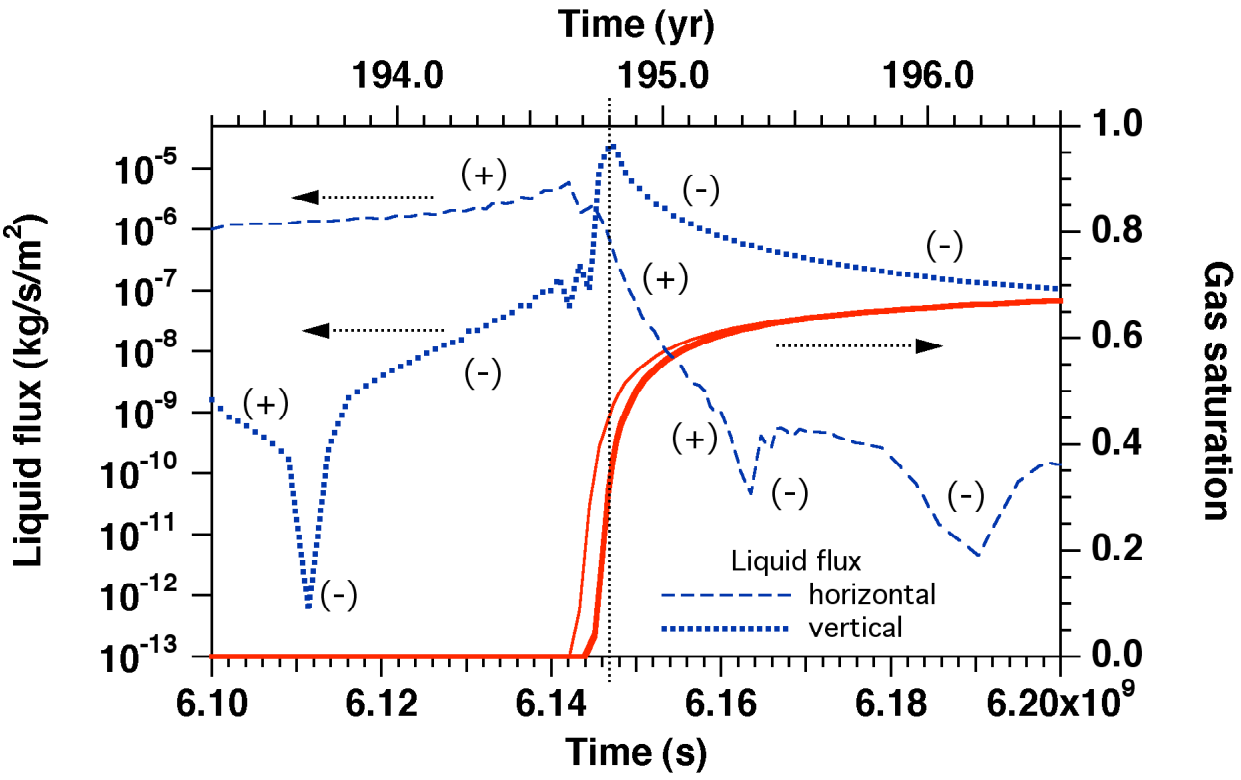

Figure 15. Horizontal and vertical aqueous phase fluxes at the top of the domain, Y = 50 km, during passage of the gas front. Gas saturations in the grid blocks located at Y = 49,995 and 50,005 m are also shown. The vertical dashed line at t = 6.147×10^9 s (194.8 yr) marks the passage of the gas front at Y = 50 km, and emphasizes maximum downflow of water at that time. Sign conventions are as follows: horizontal flow positive means updip, vertical flow positive means upward.

2.3 Dissolution and Diffusion of CO_2

The initial CO_2 inventory in the flow domain is 158.7 kt (for a section of 1 m thickness), of which only about 3.1 kt, or about 2.0 %, is dissolved in the aqueous phase. Over time the dissolved CO_2 inventory increases, reaching 14.2 kt, or 9.0 % of the total, after 13.18×10^9 s

(417.7 yr; see Fig. 16). Fig. 16 also shows free phase and dissolved CO_2 inventories for a simulation in which molecular diffusion of CO_2 in the aqueous phase was included. The diffusivity of CO_2 for the pressure and temperature conditions of interest here is approximately $D = 2 \times 10^{-9}$ m^2/s (Tewes and Boury, 2005; Farajzadeh, 2009); we use an effective diffusivity of $D_{eff} = \tau D = 10^{-9}$ m^2/s, where τ is a tortuosity coefficient assumed here as $\tau = 0.5$. It is seen that aqueous diffusion has very small effects and leads to a slight increase in dissolved CO_2, which can be understood by noting that such diffusion will transport CO_2 away from the interface between aqueous and gas phases, providing a mechanism for solubilizing additional CO_2.

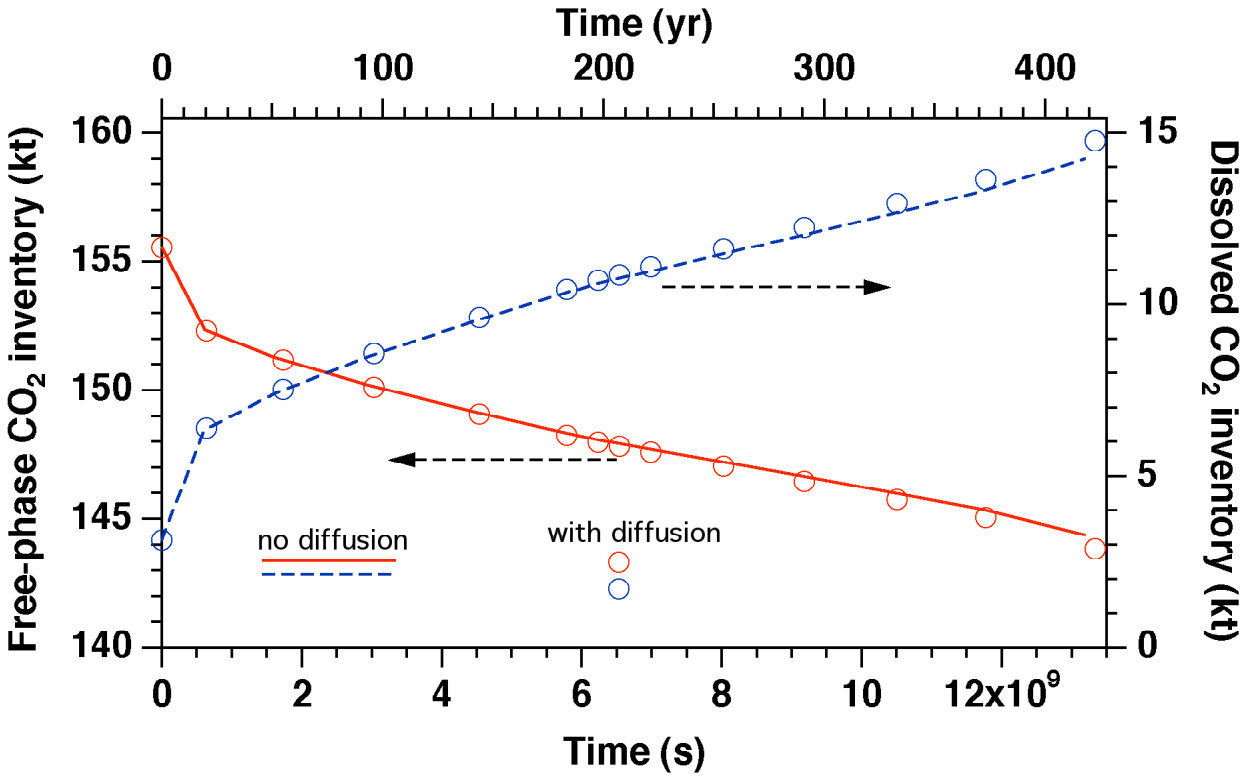

Figure 16. Time dependence of free-phase and dissolved CO_2 inventory.

Dissolution of CO_2 in the aqueous phase is subject to different effects of space discretization, that in part accelerate and in part impede such dissolution. We now proceed to a discussion of these effects.

In our simulation, when a gas phase evolves in a grid block, all aqueous phase in that grid block instantaneously acquires a dissolved CO_2 concentration corresponding to equilibrium phase partitioning at prevailing conditions of pressure, temperature, and salinity (Spycher and Pruess, 2005). In "reality," equilibrium partitioning of CO_2 and H_2O between liquid and gas phases should only occur in a region corresponding to actual plume thickness, not in discrete thickness steps determined by (sub-)vertical space discretization. Equilibrium phase partitioning in discrete steps corresponding to vertical grid resolution ΔZ will thus accelerate CO_2 dissolution. To calculate the CO_2 inventory that is solubilized due to limited vertical grid resolution, we proceed as follows. We consider that "in reality" advancing gas phase will occupy a thin layer at the top of the permeable interval. When a grid block with vertical thickness ΔZ makes a transition to two-phase conditions, gas saturation initially is very small, and aqueous phase inventory per unit footprint area can be estimated as $M_{aq} = \phi \Delta Z \rho_{aq}$. Inventory of dissolved CO_2 per unit footprint area is then $M_{dis} = \phi \Delta Z \rho_{aq} X_{aq}^{CO2}$, where X_{aq}^{CO2} is the equilibrium dissolved CO_2 mass fraction at prevailing conditions of pressure, temperature, and salinity. Applicable parameters for the problem studied here are $\phi = 0.15$, $\rho_{aq} = 1000$ kg/m^3, and $X_{aq}^{CO2} = 0.052$, yielding $M_{CO2} \approx 7.80 \Delta Z$ kg/m^2. At time t = 370.7 yr the plume extends to a distance Y = 80.5 km (Figs. 6, 8). In the intervals 15 km $\le$ Y $\le$ 35 km and 60 km $\le$ Y $\le$ 80.5 km, the bottom of the plume is in regions with a vertical grid resolution of ΔZ = 1 m, while in the intermediate region 35 km $\le$ Y $\le$ 60 km, vertical grid resolution is ΔZ = 2 m. Total dissolved CO_2 inventory in the bottommost blocks with two-phase conditions is then M_{dis} = 7.80 x (35-20 + 80.5-60)x10^3 + 7.80 x 2 x (60-35)x10^3 = 6.67x10^5 kg = 667 tonnes. This amount is negligibly small in comparison to total dissolved CO_2 inventory (Fig. 16), indicating that this type of discretization error is of minor significance.

Effects of aqueous diffusion of CO_2 away from the dissolution boundary are underestimated in our simulation, due to the relatively coarse space discretization of ΔZ = 1 m or more in the (sub-) vertical direction. At an effective diffusivity of $D_{eff} = 10^{-9}$ m^2/s, the time required for diffusion to penetrate to a depth of ΔZ can be estimated as $t = \Delta Z^2 / D_{eff}$, which for ΔZ = 1 m gives t = 10^9 s = 31.7 yr, which is significant in comparison to characteristic times of

the problem. Considerably finer discretization near the top of the domain would therefore be required to accurately resolve diffusive mass transfer.

2.4 Convectively Enhanced Dissolution

There is another effect that arises from CO_2 dissolution and subsequent diffusion, that has been neglected in the simulations presented above, and that can potentially make much larger contributions to solubilizing CO_2. As had been mentioned before, dissolution of CO_2 into aqueous phase induces an increase in aqueous phase density that, depending on salinity, is typically in the range of 1 % (for pure water) to 0.1 % (for highly saline brine). Although small, this density increase gives rise to a gravitationally unstable configuration of denser fluid above less-dense fluid. This can induce convection in the aqueous phase, which can transport CO_2 downward, away from the dissolution boundary, at much larger rates than molecular diffusion. Because of its potential relevance in accelerating CO_2 dissolution, the process of dissolution-diffusion-convection (DDC) has been studied by many investigators (Lindeberg and Bergmo, 2003; Ennis-King and Paterson, 2003a, b, 2005; Ennis-King et al., 2005; Hesse et al., 2006; Riaz et al., 2006; Xu et al., 2006; Rapaka et al., 2008; Kneafsey and Pruess, 2008). Most studies have focused on analyzing the convective instability for idealized geometries and parameters, in order to determine the onset or incubation time t_{inc} required for convection to start, and the corresponding thickness L_{inc} at which the diffusive boundary layer becomes unstable. Using linear stability analysis, Ennis-King and Paterson (2003a,b) estimated the incubation time for an isotropic medium as

$$t_{inc} = c_0 \frac{\mu^2 \phi^2 D}{(\Delta\rho)^2 g^2 k^2} \tag{3}$$

Here, μ is the aqueous phase viscosity, $\Delta\rho$ the density increase due to CO_2 dissolution, ϕ is porosity, D diffusivity, k permeability, and g acceleration of gravity. c_0 is a constant that must be determined by numerical simulation.

The relatively coarse space discretization in our large-scale model greatly limits the ability of the flow system to respond to the density increase from CO_2 dissolution. In fact,

although our simulation properly accounts for increase in aqueous phase density from CO_2 dissolution, it does not generate any buoyancy-driven aqueous phase convection over the time period simulated. This inability to accurately represent the multi-scale evolution of convective removal of dissolved CO_2 from the overlying plume causes dissolution effects to be underestimated. Here we present some estimates for the magnitude of these effects, and evaluate their relevance in predicting the fate of the CO_2 plume.

We have performed high-resolution simulations of the DDC process, using a 1m wide by 5 m tall rectangular domain (Pruess and Zhang, 2008). Vertical grid resolution was 1 mm near the top of the domain, gradually coarsening to 1 cm at larger distance from the boundary; horizontal resolution was 1 cm. By comparing CO_2 mass transfer rates with an analytical solution for diffusion only, we deduce an incubation time of 4.0×10^6 s for onset of convective activity, and a stabilized long-term CO_2 flux due to DDC of 1.0×10^{-7} kg/s/m^2 (Fig. 17). Accordingly, the DDC process will start practically instantaneously relative to characteristic time scales of plume migration.

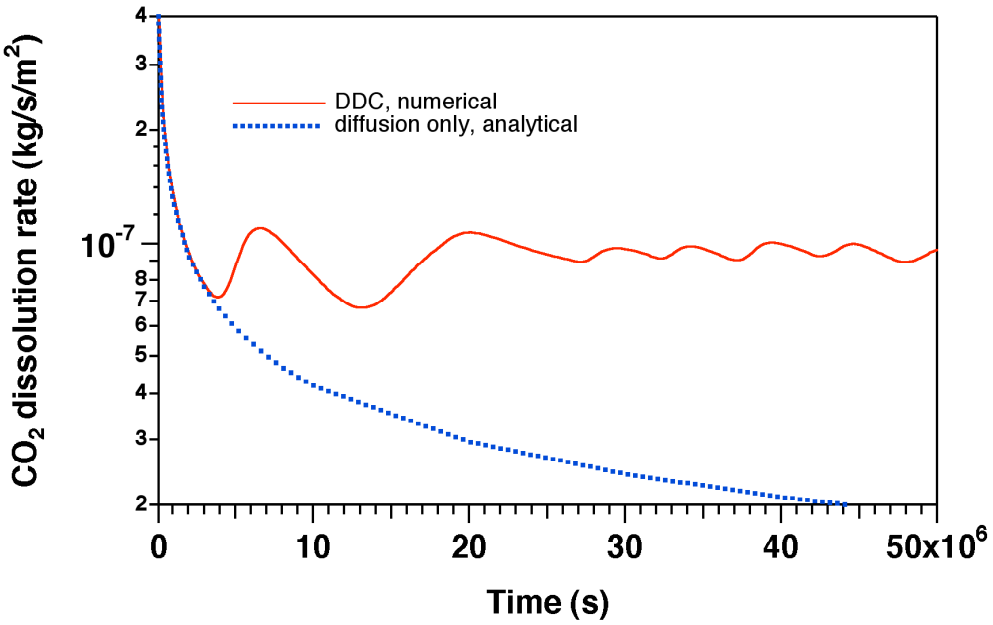

Figure 17. CO_2 dissolution rate due to convective enhancement, obtained from high-resolution simulations.

The time required for the DDC process to reach the lower boundary (Z = -200 m) of the domain can be estimated as follows. At a dissolved CO_2 mass fraction of typically 5.2 % for the conditions considered here (no salinity), an aqueous phase mass flux of $1.0x10^{-7}/0.052 = 1.923x10^{-6}$ kg/s/m^2 would be required to transmit dissolved CO_2 at a rate of $1.0x10^{-7}$ kg/s/m^2. With aqueous phase density near 1,000 kg/m^3, the corresponding volumetric flux is $1.923x10^{-9}$ m/s, and the water pore velocity is $1.923x10^{-9}/0.15 = 1.282x10^{-8}$ m/s. In the DDC process, only 1/2 of the cross-sectional area is available for downward convection, the other half being used for upward convection of water with low CO_2 and lower density. Furthermore, the dissolved CO_2 concentration in the downward convective limb is smaller than at the dissolution boundary, by a factor that based on numerical simulations we estimate as approximately 1/2 also. Accordingly, the previously estimated pore velocity of water must be increased by a factor of about 4 to achieve the DDC CO_2 flux of $1.0x10^{-7}$ kg/s/m^2. Our estimate for the convection pore velocity in the DDC process is then $4x1.282x10^{-8} = 5.128x10^{-8}$ m/s, so that the time required for significant dissolved CO_2 concentrations to reach the lower boundary (Z = -200 m) would be $200/5.128x10^{-8} = 3.90x10^9$ s = 123.6 yr.

In our high-resolution DDC simulation, CO_2-ladden water reaches the Z = - 5 m level after $1.0x10^8$ s. The process advances downward at constant speed, so that the time required to reach the Z = - 200 m level would be $(200/5)x10^8 = 4x10^9$ s, in excellent agreement with the previous, flux and concentration-based estimate. We can conclude that the DDC process will approach the lower boundary on a time scale comparable to regional plume advancement; there will be a significant time period where DDC will operate without being impacted by the lower boundary, as well as a significant time period where effects of the lower boundary will be important. During the latter time period, mass transfer rates from DDC will gradually diminish.

Let us compare the total free-phase CO_2 mass flow rate associated with plume advance with the mass transfer rate from DDC. At a time of 370.7 yr, the plume has reached a distance of Y = 80.5 km, and plume thickness at Y = 50 km is approximately 15 m (Fig. 6, bottom). The simulated sub-horizontal free-phase CO_2 flux is approximately $4x10^{-4}$ kg/s/m^2 (Fig. 10), for a total CO_2 flow rate of $6x10^{-3}$ kg/s at Y = 50 km. For a DDC flux of 10^{-7} kg/s/m^2, total rate of DDC mass transfer up to Y = 50 km would be $(50-15)x10^3x10^{-7} = 3.5x10^{-3}$ = kg/s, which is 58 %

of total free-phase flow at Y = 50 km. This indicates that DDC will have a very major impact in reducing free-phase CO_2 flow and plume advance. The coarse discretization in our regional-scale model suppresses aqueous phase convection during the time period simulated here, thereby neglecting an effect that would greatly reduce the total updip CO_2 flow rate.

3. Incorporating Convectively Enhanced Dissolution into a Field-Scale Model

As discussed above, the coarse gridding in our field-scale model suppresses CO_2 transport by means of DDC. We have implemented a first, rough treatment of sub-grid scale DDC into TOUGH2_MP/ECO2N, using the following assumptions and approximations.

1. We ignore the early-time diffusive transport and the DDC onset time of approximately 4.0×10^6 s, and assume that downward transport of CO_2 by the DDC process starts immediately when a free CO_2 phase evolves in a grid block.
2. The CO_2 flux due to DDC is applied as a sink term to the topmost row of grid blocks throughout the region with two-phase conditions.
3. DDC flux is extracted only when gas saturation exceeds a minimum value, here assumed as $S_g = S_{gr} = 0.20$.
4. DDC flux is lagged one time step, i.e., it is applied only to grid blocks that meet the DDC criteria at the beginning of a time step.
5. DDC flux is assumed constant, independent of time. Effects of the lower boundary, that would eventually reduce DDC flux on a 100 year time scale, are ignored.
6. CO_2 transported by DDC is removed from the flow domain; it is not added to the CO_2 inventory of the aqueous phase.

Approximation (1) is expected to be quite accurate, as the onset time for convection is small relative to the time scales of interest in the plume migration. Approximations (2 - 4) are expedients that avoid complications from dynamic adjustment of DDC. In "reality," DDC should remove CO_2 from the bottom rather than from the top of the plume. The approximation (2) will overestimate the amount of CO_2 removed from the upper, highly mobile portions of the plume, and will underestimate CO_2 removal from the lower portions, where gas saturations are near the

irreducible limit, and where consequently CO_2 mobility is low. Approximation (5) will lead to overestimation of DDC flux on time scales beyond 100 years. Approximation (6) ignores volumetric and convective effects that would arise from dissolution of CO_2 in the aqueous phase.

We have performed simulations of plume migration subject to DDC, assuming two different values for DDC flux, $F_{DDC} = 1x10^{-7}$ kg/s/m^2 as determined in our fine-grid simulation (Fig. 17), and a value half this large, $F_{DDC} = 0.5x10^{-7}$ kg/s/m^2, to explore the sensitivity to reduced vertical permeability. Fig. 18 compares results for the CO_2 plumes after about 335 years with the previous simulation that ignored DDC. It is seen that the main effect of DDC is to reduce the thickness of the upper, highly mobile portions of the plume, while impacts on the advancement of the plume appear to be minor. A plot of plume advancement versus time indeed shows that plume advancement is essentially unaffected by CO_2 solubilization due to DDC (Fig. 19). This result may appear surprising at first, but it is consistent with the observations on plume behavior in Sec. 2, above. Indeed, we found that gas saturations and updip CO_2 fluxes are essentially constant throughout the mobile portion of the plume, and that rate of plume advance is constant, independent of plume thickness. The DDC process affects (reduces) the thickness of the highly mobile portion of the plume, but does not affect CO_2 flux in the mobile portion.

Could our finding of constant speed of plume advancement be at least partially due to the admittedly crude approximations made in our implementation of sub-grid-scale DDC? Our approximations cause CO_2 to be removed from the upper, mobile portion of the plume, whereas DDC should primarily affect the lower, barely mobile portion. Accordingly, our implementation of DDC actually overestimates impacts on the mobile portion, and should overestimate impacts on plume advancement. The absence of a reduction in the speed of plume advancement even when making an approximation that would overestimate such effects is strong evidence that plume advancement indeed is not affected by DDC. The only impact is a reduction in the thickness of the mobile portion of the plume, with a concomitant reduction in total CO_2 flow rate, which is proportional to mobile plume thickness. We expect that a more accurate model for DDC will predict less reduction in mobile plume thickness, while removing more CO_2 from the lower, poorly mobile portions of the plume, so that the two-phase boundary would be shifted upward.

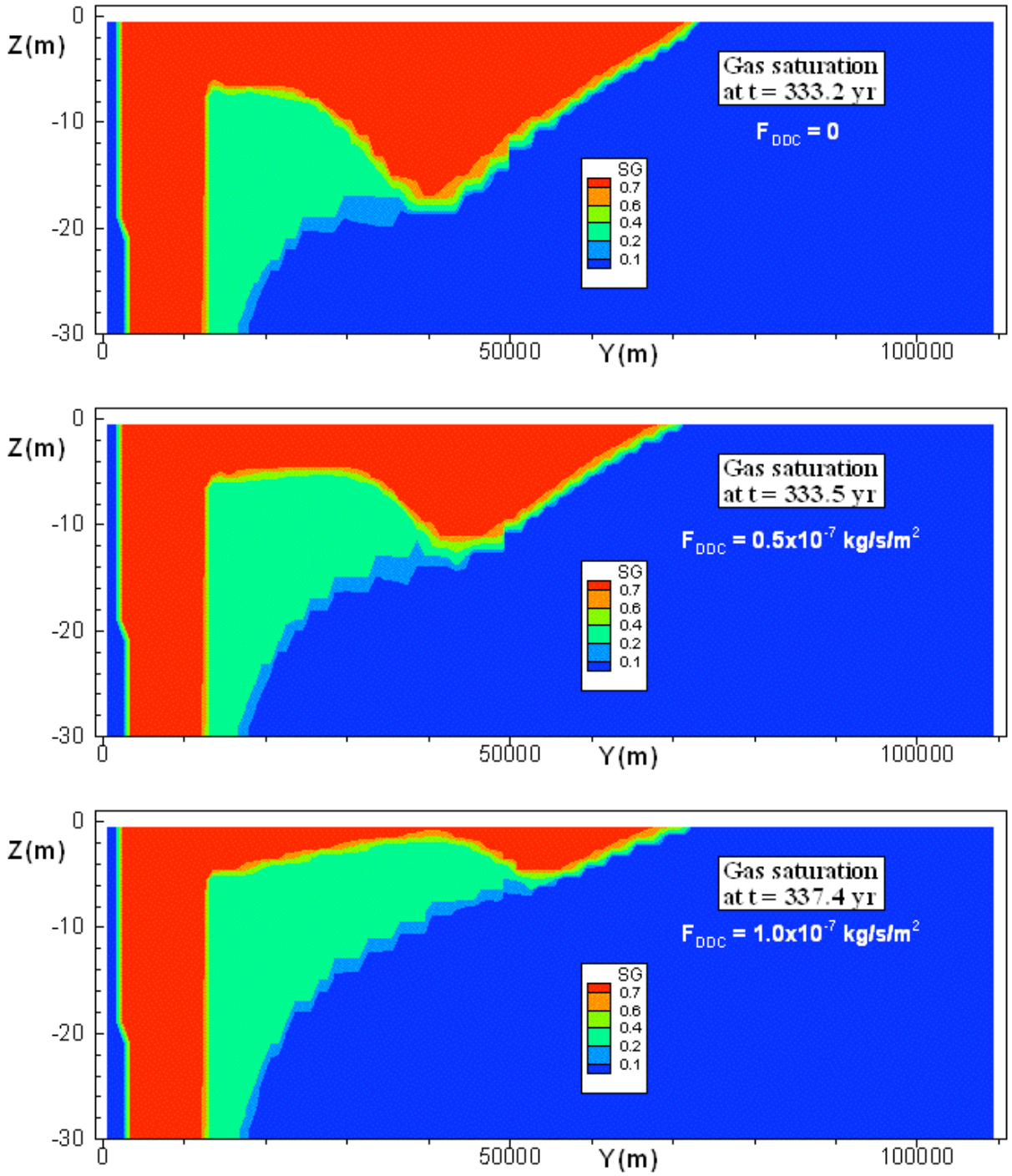

Figure 18. Gas saturations after approximately 335 years for different strengths of the dissolution-diffusion-convection (DDC) process.

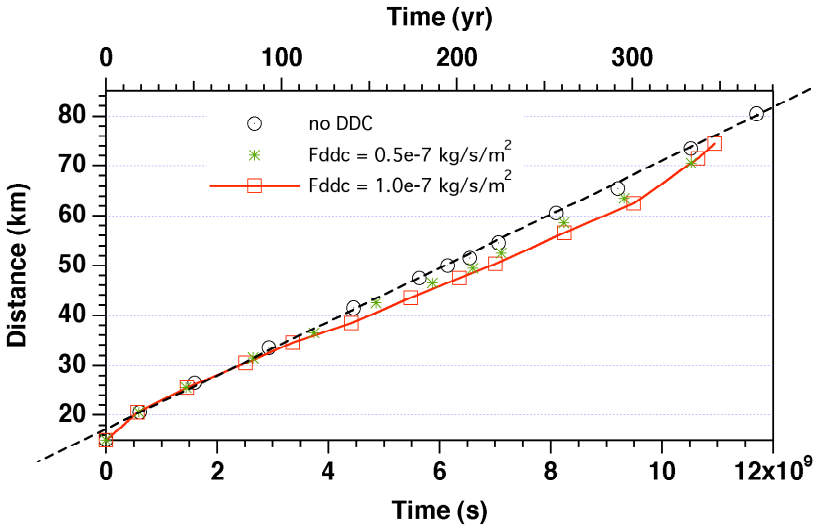

Figure 19. Plume advancement versus time for different strengths of DDC flux.

Mass balances for free-phase and dissolved CO_2 show substantial increase in CO_2 solubilization from DDC (Fig. 20). In plotting Fig. 20, we included the free-phase CO_2 removed by our sub-grid-scale representation of DDC as dissolved CO_2. For the case with $F_{DDC} = 1x10^{-7}$ kg/s/m^2, at the end of the simulation approximately 1/3 of the initial CO_2 inventory has been dissolved into the aqueous phase, while 2/3 remain as a free supercritical phase.

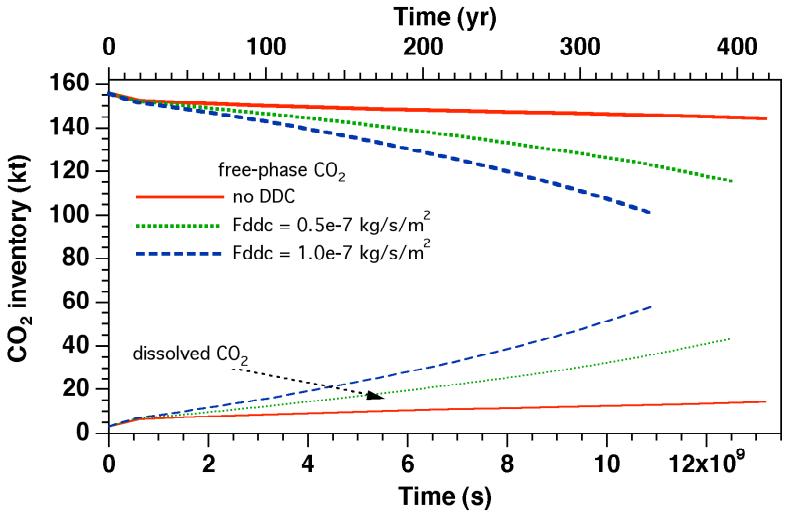

Figure 20. Free-phase and dissolved CO_2 inventory for different strengths of DDC.

4. Concluding Remarks

The migration of a CO_2 plume under a sloping caprock involves processes on a wide range of space and time scales, posing difficult challenges for numerical modeling. We have used the TOUGH2_MP/ECO2N simulator on a plume migration problem whose parameters were chosen to be applicable to the Carrizo-Wilcox aquifer in Texas. Plume behavior was simulated for a time period of a few hundred years, and covering a migration distance of order 100 km. In addition, we performed high-resolution simulations of the convective instability that develops when CO_2 dissolves and diffuses into aqueous phase, increasing fluid density, and inducing convective enhancement of CO_2 dissolution. Our main findings are as follows.

- Gas saturations in the upper portion of the advancing CO_2 plume are nearly uniform, and updip migration occurs at constant speed, independent of plume thickness.
- The mechanism of plume advancement is quite different from displacement behavior in the vicinity of an injection well. Near a CO_2 injection well, the plume advances by pressure-driven displacement of aqueous phase away from the injection point. In contrast, at the tip of a CO_2 plume advancing under a sloping caprock, water flow is mostly downward rather than outward. One can say that the plume advances updip due to a collapse of the water column ahead of the plume tip, induced by the approaching smaller vertical pressure gradient in the CO_2 plume.
- In a coarsely-gridded field-scale model, the process of dissolution and diffusion of CO_2 into the aqueous phase does not give rise to convective mixing, because the large scale of spatial averaging suppresses the convective instability.
- High-resolution simulations have shown that the process of CO_2 dissolution-diffusion-convection (DDC) gives rise to CO_2 dissolution at an enhanced rate that stabilizes over time.
- A first rough model for subgrid-scale DDC was implemented into TOUGH2-MP, and was used to explore the impact of DDC on long-term behavior of the plume. The results showed that convectively enhanced dissolution made the advancing CO_2 plume thinner, and reduced the updip CO_2 flow rate. Surprisingly, it did not affect the speed of plume advancement.

The simulations presented here did not include hysteresis in relative permeability and ignored capillary pressures. Hysteretic effects are known to be important for long-term trapping of CO_2 (Doughty, 2007), and will be explored in the future, as will effects of capillary pressure.

Acknowledgement

I would like to thank Jan Nordbotten and Helge Dahle for stimulating discussions. Thanks are due to Christine Doughty and Curt Oldenburg for a careful review of the manuscript and the suggestion of improvements. This work was supported by the Office of Basic Energy Sciences and by the Zero Emission Research and Technology project (ZERT) under Contract No. DE-AC02-05CH11231 with the U.S. Department of Energy.

References

Corey, A.T. The Interrelation Between Gas and Oil Relative Permeabilities, *Producers Monthly*, pp. 38 - 41, November 1954.

Doughty, C. Modeling Geologic Storage of Carbon Dioxide: Comparison of Non-hysteretic and Hysteretic Characteristic Curves, *Energy Conv. Managmt.,* Vol. 48, pp. 1768–1781, 2007.

Ennis-King, J. and L. Paterson. Rate of Dissolution due to Convective Mixing in the Underground Storage of Carbon Dioxide, in J. Gale and Y. Kaya (Eds.), *Greenhouse Gas Control Technologies,* Volume 1, pp. 507–510, Elsevier, 2003a.

Ennis-King, J. and L. Paterson. Role of Convective Mixing in the Long-Term Storage of Carbon Dioxide in Deep Saline Formations, paper SPE-84344, presented at *Society of Petroleum Engineers Annual Fall Technical Conference and Exhibition,* Denver, CO, October 2003b.

Ennis-King, J. and L. Paterson. Role of Convective Mixing in the Long-Term Storage of Carbon Dioxide in Deep Saline Formations, *SPE Journal,* pp. 349–356, September 2005.

Ennis-King, J., I. Preston and L. Paterson. Onset of Convection in Anisotropic Porous Media subject to a rapid change in boundary conditions, *Phys. of Fluids,* Vol. 17, 084107, DOI: 10.1063/1.2033911, 2005.

Farajzadeh, R. Enhanced Transport Phenomena in CO2 Sequestration and CO2 EOR, PhD thesis, Technical University Delft, The Netherlands, 2009.

Hesse, M.A., H.A. Tchelepi and F.M. Orr, Jr. Natural Convection During Aquifer CO2 Storage, presented at GHGT-8, *8th International Conference on Greenhouse Gas Control Technologies,* Trondheim, Norway, June 2006.

Hesse, M.A., F.M. Orr, Jr., and H.A. Tchelepi. Gravity Currents with Residual Trapping, *J. Fluid Mech.,* Vol. 611, pp. 35–60, 2008.

IPCC (Intergovernmental Panel on Climate Change), Special Report on Carbon Dioxide Capture and Storage, 2005.

Kneafsey, T.J. and K. Pruess. Laboratory Flow Experiments for Visualizing Carbon Dioxide-Induced, Density-Driven Brine Convection, submitted to *Transport in Porous Media,* December 2008.

Kumar, A., M. Noh, G.A. Pope, K. Sepehrnoori, S. Bryant and L.W. Lake. Reservoir Simulation of CO2 Storage in Deep Saline Aquifers, paper SPE-89343, presented at *Society of Petroleum Engineers Fourteenth Symposium on Improved Oil Recovery,* Tulsa, OK, April 2004.

Lindeberg, E. and P. Bergmo. The Long-Term Fate of CO2 Injected into an Aquifer, in: J. Gale and Y. Kaya (eds.), *Greenhouse Gas Control Technologies,* pp. 489–494, Elsevier Science, Ltd., Amsterdam, The Netherlands, 2003.

Nicot, J.-P. Evaluation of Large-Scale CO_2 Storage on Fresh-Water Sections of Aquifers: An Example from the Texas Gulf Coast Basin, *Int. J. Greenhouse Gas Control,* Vol. 2, Issue 4, pp. 583–593, 2008.

Pau, G.S.H., A.S. Almgren, J.B. Bell and M.J. Lijewski. A Parallel Second-Order Adaptive Mesh Algorithm for Incompressible Flow in Porous Media, submitted to *Proc. Royal Soc. A,* 2009.

Pruess, K. The TOUGH Codes—A Family of Simulation Tools for Multiphase Flow and Transport Processes in Permeable Media, *Vadose Zone J.,* Vol. 3, pp. 738 - 746, 2004.

Pruess K. and N. Spycher. ECO2N – A Fluid Property Module for the TOUGH2 Code for Studies of CO2 Storage in Saline Aquifers, *Energy Conversion and Management,* Vol. 48, No. 6, pp. 1761–1767, doi:10.1016/j.enconman.2007.01.016, 2007.

Pruess, K. and K. Zhang. Numerical Modeling Studies of The Dissolution-Diffusion-Convection Process During CO2 Storage in Saline Aquifers, Lawrence Berkeley National Laboratory report LBNL-1243E, November 2008.

Rapaka, S., S. Chen, R.J. Pawar, P.H. Stauffer and D. Zhang. Non-modal Growth of Perturbations in Density-driven Convection in Porous Media, *J. Fluid Mech.,* Vol. 609, pp. 285–303, 2008.

Riaz, A., M. Hesse, H.A. Tchelepi and F.M. Orr Jr. Onset of Convection in a Gravitationally Unstable Diffusive Boundary Layer in Porous Media, *J. Fluid Mech.,* Vol. 548, pp. 87–111, 2006.

Spycher, N. and K. Pruess. CO_2-H_2O Mixtures in the Geological Sequestration of CO_2. II. Partitioning in Chloride Brines at 12–100 °C and up to 600 bar, *Geochim. Cosmochim. Acta,* Vol. 69, No. 13, pp. 3309–3320, doi:10.1016/j.gca.2005.01.015, 2005.

Tewes, F. and F. Boury. Formation and Rheological Properties of the Supercritical CO2–Water Pure Interface, *J. Phys. Chem. B,* Vol. 109, No. 9, pp. 3990–3997, 2005.

van Genuchten, M.Th. A Closed-Form Equation for Predicting the Hydraulic Conductivity of Unsaturated Soils, *Soil Sci. Soc. Am. J.*, Vol. 44, pp. 892 - 898, 1980.

Xu, X., S. Chen and D. Zhang. Convective Stability Analysis of the Long-term Storage of Carbon Dioxide in Deep Saline Aquifers, *Adv. Wat. Resour.,* Vol. 29, pp. 397–407, 2006.

Zhang, K., Y.S. Wu and K. Pruess. User's Guide for TOUGH2-MP - A Massively Parallel Version of the TOUGH2 Code, Lawrence Berkeley National Laboratory Report LBNL-315E, May 2008.